21

Magnetically Tunable Unidirectional Electromagnetic Devices Based on Magnetic Surface Plasmon

Shiyang Liu[1], Huajin Chen[1], Zhifang Lin[2] and S. T. Chui[3]
[1]*Institute of Information Optics, Zhejiang Normal University*
[2]*State Key Laboratory of Surface Physics (SKLSP) and Department of Physics, Fudan University*
[3]*Department of Physics and Astronomy, University of Delaware*
[1,2]*China*
[3]*USA*

1. Introduction

Plasmonic metamaterials are composite, artificial materials, consisting of metallic resonant building blocks designed with state-of-the-art configurations. Many exotic phenomena not occurring in nature such as negative refraction (Burgos et al., 2010; Dolling et al., 2006; Lezec et al., 2007; Liu et al., 2008; Pendry, 2000; Shalaev, 2007; Shelby et al., 2001; Smith et al., 2000; Valentine et al., 2008; Veselago, 1968; Zhang et al., 2005), subwavelength imaging (Fang et al., 2005; Liu et al., 2007; Pendry, 2000; Taubner et al., 2006), cloaking (Ergin et al., 2010; Leonhardt, 2006; Lai et al., 2009; Li et al., 2008; Liu et al., 2009; Pendry et al, 2006; Schurig et al., 2006), and so on can be observed in the systems made of such materials. A particular characteristic of the system is the excitation of surface plasmon polaritons (SPPs) (Barnes et al., 2003; Giannini et al., 2010; Noginov et al., 2008; Zayats et al., 2005), which originates from the coupling of the electromagnetic (EM) wave to the free electron oscillation in metallic surface. The EM waveguiding mediated by the SPPs has gained more and more attention from theorists, experimentalists, and engineers due to its promising applications in integrated optical circuit, optical storage, biosensing, and even medical therapy (Engheta, 2007; Ozbay, 2006; Zia et al., 2006). A series of plasmonic components have been proposed and realized, such as plasmonic waveguides, beam splitter, sharp bends and so on. Very recently, based on the excitation of the SPPs the plasmonic Luneburg and Eaton lens are even realized experimentally (Zentgraf, 2011).

So far, plasmonics relevant phenomena have been extensively investigated from both the theoretical and the experimental perspectives. The symmetry of the Maxwell's equations with respect to its electric and magnetic part suggests that the magnetic analogue of the surface plasmon, "magnetic surface plasmon" (MSP) (Gollub et al., 2005; Liu et al., 2008), can also be excited. It originates from the coupling of EM wave to the collective resonance of spin wave, and thus can be observed in the magnetic system. However, the relevant issues are not examined elaborately as the case for the surface plasmon in metallic materials. In addition, there appeared burgeoning activities in exploring the phenomena resulting from the time

reversal symmetry (TRS) breaking for photons. Among others, the EM one-way edge modes analogous to quantum Hall edge states were discussed by Haldane and Raghu (Haldane & Raghu, 2008), and later by Wang and co-workers (Wang et al., 2008; 2009). Recently, the self-guiding unidirectional EM edge states are also realized theoretically (Ao et al., 2009) and experimentally (Poo et al., 2011). In the metamaterials designed with ferrite materials, the magnetic response is intrinsic, accordingly, termed as magnetic metamaterials (MMs), where the MSP resonance can be excited. Besides, the TRS breaking relevant phenomenon for the photons can also be observed (Liu et al., 2010; 2011; Wang et al., 2008). In particular, we can find that the MMs can mold the reflection in a dramatic manner (Liu et al., 2011).

Similar to the electric surface plasmon (ESP) resonance occurring when its permittivity $\varepsilon = -1$ in metallic rod. For a ferrite rod, the MSP resonance occurs when its effective permeability $\mu = -1$ (Liu et al., 2008). Due to the TRS breaking nature in ferrite materials, there exist unequal amounts of states with opposite angular momenta for the scattered field. Near the MSP resonance, the angular momenta contents are dominated by one sign, with that for the other sign almost completely suppressed. Accordingly, a giant circulation (clockwise or anticlockwise) of energy flow develops, so only the energy flow in one direction is supported (Chui & Lin, 2007). Consequently, in this work we consider the phenomenon resulting from the combined action of the MSP resonance and the TRS breaking (Liu et al., 2011). In addition, the working frequency can be controlled by an external magnetic field (EMF), facilitating the design of the practical EM devices.

The present chapter is organized as follows. In the second part, we give a brief introduction on the Mie theory on the ferrite rod and the multiple scattering theory used in the numerical simulations. Then, we present the reflection behavior due to the MSP resonance and its physical origin. The dependence of the behavior on the working frequency and the source-interface separation is also examined. Following this part, we show a design of a one-way EM waveguide (OEMW) based on this effect. Most importantly, the robustness of the OEMW against defect, disorder, and inhomogeneity of the EMF are examined. The manipulability of the working frequency is demonstrated as well by tuning the EMF. Some other complicate EM devices such as a sharp beam bender and a beam splitter are also designed. In addition, all the designed EM devices are shown to be operable even in the deep subwavelength scale. Our results are summarized in the conclusion part.

2. Theoretical approach

To design the MM, we use single crystal yttrium-iron-garnet (YIG) ferrite rods as building blocks. In our case, the ferrite rods are arranged periodically as a square lattice in the air with lattice constant a and the radius of the ferrite rod r_s. The rod axis are oriented along the z direction, corresponding to the direction of the EMF. When fully magnetized, the magnetic permeability can be written in the form (Pozar, 2004; Slichter, 1978)

$$\widehat{\mu} = \begin{pmatrix} \mu_r & -i\mu_\kappa & 0 \\ i\mu_\kappa & \mu_r & 0 \\ 0 & 0 & 1 \end{pmatrix}, \qquad \widehat{\mu}^{-1} = \begin{pmatrix} \mu_r' & -i\mu_\kappa' & 0 \\ i\mu_\kappa' & \mu_r' & 0 \\ 0 & 0 & 1 \end{pmatrix}, \tag{1}$$

with

$$\mu_r = 1 + \frac{\omega_m(\omega_0 - i\alpha\omega)}{(\omega_0 - i\alpha\omega)^2 - \omega^2}, \quad \mu_\kappa = \frac{\omega_m\omega}{(\omega_0 - i\alpha\omega)^2 - \omega^2}, \quad \mu_r' = \frac{\mu_r}{\mu_r^2 - \mu_\kappa^2}, \quad \mu_r' = \frac{-\mu_\kappa}{\mu_r^2 - \mu_\kappa^2},$$

where $\omega_0 = \gamma H_0$ is the resonance frequency with $\gamma = 2.8$ MHz/Oe the gyromagnetic ratio; H_0 the sum of the EMF applied in z direction and the shape anisotropy field (Pozar, 2004), $\omega_m = 4\pi\gamma M_s$ is the characteristic frequency with $4\pi M_s = 1750$ Oe the saturation magnetization, and α is the damping coefficient of the ferrite. In the calculation of photonic band diagram, we set $\alpha = 0$ (Wang et al., 2008), and in the simulation $\alpha = 3 \times 10^{-4}$. The relative permittivity of the ferrite rods is taken as $\varepsilon = 15 + 3 \times 10^{-3} i$. In our work, the transverse magnetic (TM) mode is considered.

To make our results reliable and convergent efficiently, we have used the Mie theory to solve the scattering properties of a single ferrite rod. For an incident EM wave with TM polarization, it can be expanded into vector cylindrical wave functions (VCWFs) (Bohren & Huffman, 1983)

$$\boldsymbol{E}_0(j) = \sum\nolimits_n E_n q_n^{(j,j)} \boldsymbol{N}_n^{(1)}(k_b, \boldsymbol{r}_j), \tag{2}$$

where j suggests that the $j-$th coordinate is used, indicating that the EM fields are expanded around the $j-$th ferrite rod, $\boldsymbol{N}_n^{(1)}(k_b, \boldsymbol{r}_j)$ is the VCWF with k_b the wavenumber in the background medium, satisfying $k_b^2 = \omega^2 \varepsilon_b \mu_b$, ε_b and μ_b correspond, respectively, to the permittivity and permeability of the background medium, $E_n = i^n |E_0|$ with $|E_0|$ the amplitude of the incident EM wave. For plane wave, the expansion coefficients can be easily obtained

$$q_n^{(j,j)} = e^{-in\phi_\kappa} \exp(i\boldsymbol{k}_b \cdot \boldsymbol{d}_{0j}), \tag{3}$$

where $\boldsymbol{k}_b = \kappa \cos\phi_\kappa \boldsymbol{e}_x + \kappa \sin\phi_\kappa \boldsymbol{e}_y$ is the wave vector of the incident EM wave with $\kappa = |\boldsymbol{k}_b|$, $\boldsymbol{d}_{0j} = \boldsymbol{r} - \boldsymbol{r}_j$, corresponding to the position of the $j-$th ferrite rod in the $0-$th coordinate. The scattered EM wave can be expanded into VCWFs as well in the form

$$\boldsymbol{E}_s(j) = -\sum\nolimits_n E_n b_n^{(j,j)} \boldsymbol{N}_n^{(3)}(k_b, \boldsymbol{r}_j), \tag{4}$$

In Eqs. (2) and (4), the VCWFs are defined according to

$$\boldsymbol{N}_n^{(J)}(k, \boldsymbol{r}) = z_n^{(J)}(kr) e^{in\phi} \boldsymbol{e}_z, \tag{5}$$

where

$$z_n^{(J)}(kr) = \begin{cases} J_n(kr) & \text{for } J = 1, \\ H_n^{(1)}(kr) & \text{for } J = 3, \end{cases} \tag{6}$$

In Eq. (6), $J_n(kr)$ and $H_n^{(1)}(kr)$ correspond, respectively, to the first kind of Bessel function and the first kind of Hankel function.

The EM wave inside the ferrite rod can also be expanded into VCWFs, but the form is so complicated. Therefore, to save the space we do not give the corresponding result. By matching the boundary conditions, we can solve the problem and obtain the Mie coefficients, which can connect the unknown scattering coefficients with the given expansion coefficients of the incident wave in the form

$$b_n^{(j,j)} = \mathcal{S}_n^{(j)} q_n^{(j,j)}, \tag{7}$$

where $\mathcal{S}_n^{(j)}$ is the Mie coefficients of the $j-$th ferrite rod (Chen et al., 2007; Chui & Lin, 2007; Eggimann, 1960)

$$\mathcal{S}_n = \frac{\frac{\mu_s}{\mu_b} J_n'(x) - J_n(x) \left[\frac{m_s^2}{m_s'} D_n(m_s' x) + \frac{n\mu_k'}{x} \right]}{\frac{\mu_s}{\mu_b} H_n^{(1)\prime}(x) - H_n^{(1)}(x) \left[\frac{m_s^2}{m_s'} D_n(m_s' x) + \frac{n\mu_k'}{x} \right]}. \tag{8}$$

In Eq. (8), the superscripts "′" of $J_n(x)$ and $H_n(x)$ denote the derivatives with respect to the argument $x = k_b r_s$, the other parameters $k_s^2 = \omega^2 \epsilon_s \mu_s$, $m_s = k_s/k_b$, $m_s' = m_s/\sqrt{\mu_r'}$, and $D_n(m_s' x) = J_n'(m_s' x)/J_n(m_s' x)$.

By combining the Mie theory with the multiple scattering theory (Felbacq et al., 1994; Leung & Qiu, 1993; Liu & Lin, 2006; Wang et al., 1993), we can handle the scattering problem for a system consisting of multiple ferrite rods. Then, the scattering coefficients around each ferrite rod can be obtained by solving the linear equations

$$b_n^{(j)} = \mathcal{S}_n^{(j)} \left[q_n^{(j,j)} - \sum_{l \neq j} \sum_m A_{nm} b_m^{(l)} \right]. \tag{9}$$

In Eq. (9), A_{nm} is the translational coefficient (Chew, 1995)

$$A_{nm} = i^{n-m} H_{n-m}^{(1)}(k d_{lj}) \exp\left[-i(n-m)\phi_{lj} \right], \tag{10}$$

where $\boldsymbol{d}_{lj} = \boldsymbol{r}_l - \boldsymbol{r}_j$ and (d_{lj}, ϕ_{lj}) is the polar coordinate of the position vector $\boldsymbol{d}_{lj}$. By setting $q_n^{(j,j)} = 0$ and find the corresponding eigenmodes, we can also calculate the photonic band diagrams.

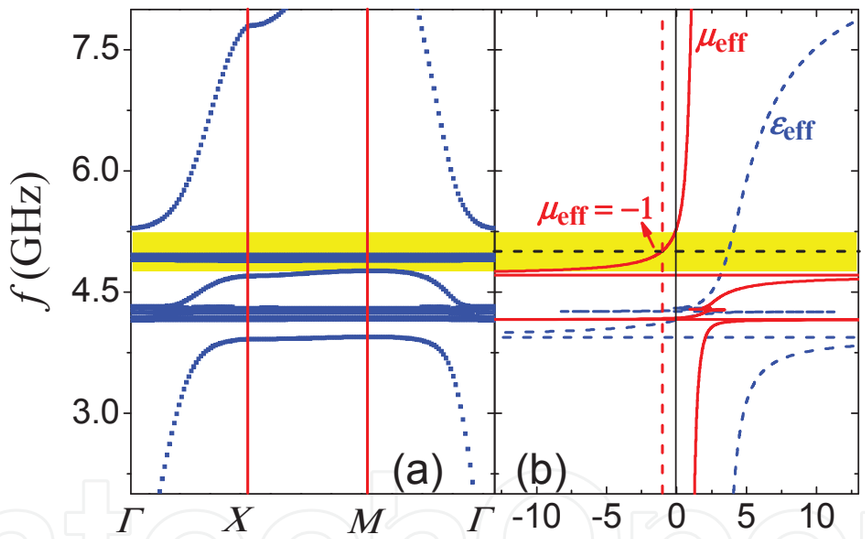

Fig. 1. (a) The photonic band diagram for an MM of square lattice with lattice constant $a = 8$ mm and under an EMF of $H_0 = 900$ Oe. (b) The retrieved effective constitutive parameters where the blue dashed line and red solid line correspond to the effective permittivity ε_{eff} and the effective magnetic permeability μ_{eff}, respectively.

3. MSP resonance in MM

The MM considered are made of single crystal YIG rods arranged periodically in a square lattice with the lattice constant $a = 8$ mm and the rod radius $r = \frac{1}{4}a = 2$ mm. Firstly, let's examine the origin of the MSP resonance. It depends on the resonance of the each single ferrite rod. The coupling of the neighboring MSP resonant states of each single ferrite rod results in the resonance of the whole system. For a ferrite rod with the permeability given by Eq. (1),

the MSP resonance occurs at a frequency

$$f_s = \frac{1}{2\pi}\left(\omega_0 + \frac{1}{2}\omega_m\right), \tag{11}$$

corresponding to the case when $\mu_r + \mu_\kappa = -1$ (Liu et al., 2008), which can be regarded as the effective permeability of a single ferrite rod. In the present case, the applied EMF field is such that $H_0 = 900$ Oe, yielding a MSP resonance at $f_s = 4.97$ GHz. To gain a better understanding of the MSP resonance, we present the photonic band diagram in Fig. 1 (a). At the working frequency $f = 5$ GHz (corresponding the wavelength 60 mm) the wavelength is nearly 8 times of the lattice constant a so that the MM can be considered as an effective medium. With the effective-medium theory developed in our previous work (Jin et al., 2009), we can retrieve the effective permeability tensor,

$$\mu_e = \begin{pmatrix} \mu & -i\mu' & 0 \\ i\mu' & \mu & 0 \\ 0 & 0 & 1 \end{pmatrix}. \tag{12}$$

Then, the effective permeability μ_{eff} for TM mode is given by $(\mu^2 - \mu'^2)/\mu$, which is shown in Fig. 1(b). By comparing the photonic band diagram and the effective constitutive parameters μ_{eff} and ε_{eff}, we can find that double positive effective parameters correspond to the photonic bands, single negative effective parameter corresponds to the photonic band gap (PBG) , while the resonances correspond to the flat bands. Near the frequency corresponding to the flat bands in Fig. 1(b) (at the MSP resonance frequency $f_s = 4.97$ GHz) the effective magnetic permeability is nearly equal to -1 as is marked by the black dashed line, consistent with the analysis on the single ferrite rod. For this reason, the MSP resonance can be considered as the magnetic analogue of the surface plasmon resonance inhabited in the metallic materials. In addition, around the MSP resonance two PBGs come into existence as denoted by the yellow stripes in Fig. 1(a) where $\mu_{\text{eff}} < 0$, in the vicinity of the MSP resonance. This is also the working frequency range we select to examine the corresponding reflection behavior.

4. Molding reflection with MM slab

To explore the physical consequence resulting from the combined action of the MSP resonance and the TRS breaking, we have examined the reflection behavior of a TM wave excited by a line source working at a frequency near f_s and located near an MM slab. Typical results are demonstrated in Fig. 2, where the line source oscillating at $f = 5$ GHz is located a distance $a = 8$ mm away from a four-layer MM slab. The total electric field, the scattered electric field, together with the x-component of the Poynting vector are plotted in panels (a), (b), and (c), respectively, where a sharply asymmetric reflection (SAR) can be observed. On the left hand side (LHS) of the line source, the scattered field substantially cancels the incoming field, resulting in a darkened region near the MM surface. On the right hand side (RHS) of the line source, the scattered field significantly enhances the EM field, giving rise to a brightened region near the MM surface. Since the working frequency is selected in the PBG as can be seen from the photonic band diagram in Fig. 1 (a), the EM wave can not propagate inside the MM slab. The vanishment of the total field inside the MM slab indicates that the incident and scattered fields inside the MM have a π phase difference. For the scattered wave, on the LHS of the line source, the bright fringes both inside and outside the MM [shown in Fig. 2 (b)] remains at the same positions. This indicates that the scattered waves on the LHS are continuous in phase near the surface of MM. As the scattered field cancels the incident field

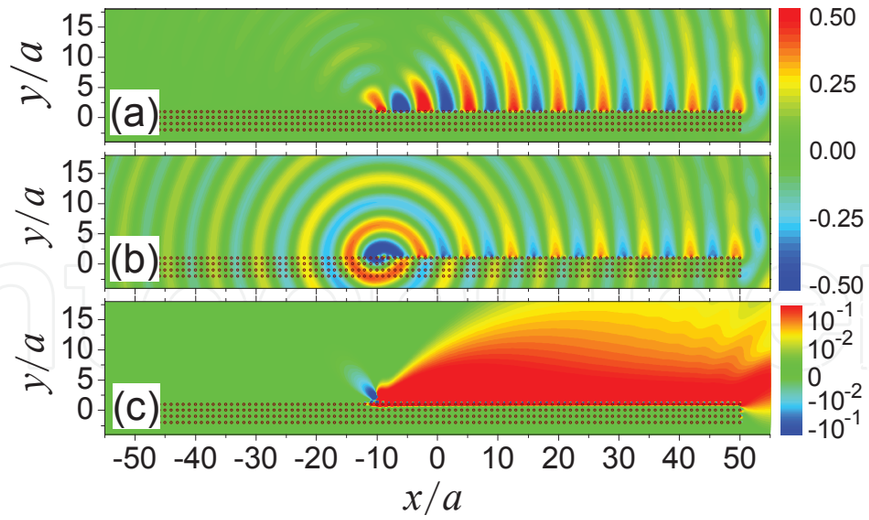

Fig. 2. The patterns of the total electric field (a), the scattered electric field (b), and the x-component of the Poynting vector (c) for a line source operating at a frequency $f = 5$ GHz close to the MSP resonance. The lattice constant of the MM slab is $a = 8$ mm and the line source is located $1.0a$ away from the surface of the MM slab.

inside the MM slab, it therefore also attenuates the incident field outside the MM slab. The situation is quite different on the RHS of the line source. As can be seen from Fig. 2 (b), the bright fringe outside the MM slab is at the same position as the dark fringe inside the MM slab near the interface. There appears a nearly half-wavelength mismatch for scattered waves inside and outside the MM slab. This suggests a phase change around π occurs inside and outside the MM slab. As a consequence, while the scattered field cancels the incident field inside the slab due to the phase mismatch, it considerably enhances the EM field near surface outside the MM slab owing to in-phase interference. In this manner, we can understand the SAR effect phenomenologically.

As can be seen from Fig. 1, the working frequency is selected near the MSP resonance, which plays a crucial role for the phenomenon occurring in the system. The excitation of the MSP resonance can lead to the appearance of the unidirectional circulation of the energy flow as schematically shown in Fig. 3. Accordingly, for a line source located near the surface of the MM slab, the leftward energy flow is inhibited while the rightward energy flow is supported

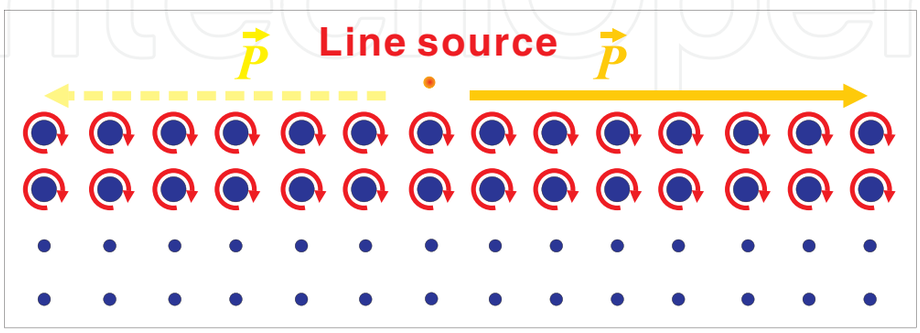

Fig. 3. The simple physical picture illustrating the excitation of the one-way circulating MSP band states, which is responsible for the occurrence of the SAR effect shown in Fig. 2.

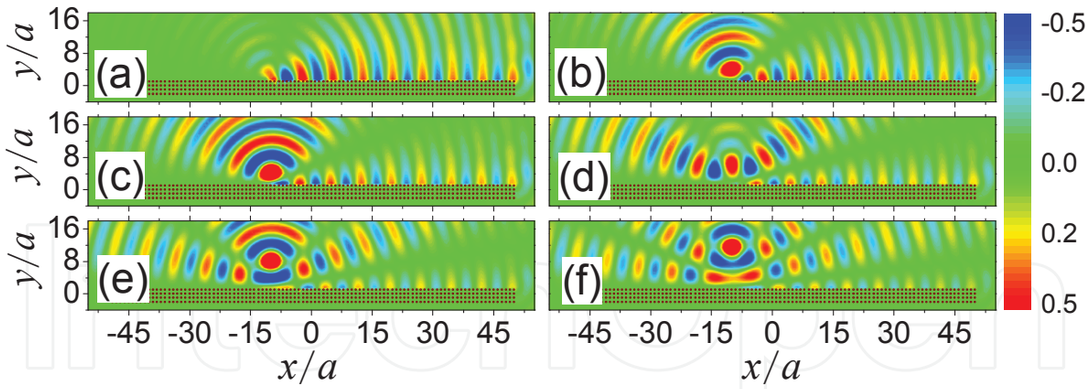

Fig. 4. The electric field patterns showing the SAR effect corresponding to different source-interface separations d. Panels (a), (b), (c), (d), (e), and (f) correspond to the cases when $d = 1a$, $2a$, $3a$, $5a$, $7a$, and $10a$, respectively. All the other parameters are the same as those in Fig. 1. The working frequency is selected at $f = 5$ GHz. The MM slab is the same as that in Fig. 2.

and reinforced. For this reason, we can observe the SAR effect shown in Fig. 2. Interestingly, by reversing the orientation of the EMF the circulation of the energy flow can also be reversed. Therefore, the EM property relevant to the SAR effect is magnetically tunable.

4.1 Separation dependence of the SAR effect

As aforementioned, the SAR effect originates from the MSP resonance. Therefore, it is necessary to examine the dependence of the SAR effect on the source-interface separation d. The corresponding results are shown in Fig. 4 where panels (a), (b), (c), (d), (e), and (f) correspond to the electric field patterns when $d = 1a$, $2a$, $3a$, $5a$, $7a$, and $10a$, respectively. The operating frequency is $f = 5$ GHz, all the other parameters of the MM slab are also the same as those in Fig. 2. When the line source is close to the interface of MM slab a dramatic SAR effect can be observed. With the increase of the separation d, the SAR effect becomes weaker and weaker, namely, more and more electric field is scattered into the outside space. When the line source is far enough from the interface ($d \approx \lambda$), the electric field near the interface becomes very weak and the electric field pattern is nearly symmetric as can be observed in Figs. 4 (e) and (f). This result can be understood from the following approximate physical picture. The incoming electric field at a position $\boldsymbol{r}$ is given by

$$E_i(\boldsymbol{r}) = \exp[i\boldsymbol{k}\cdot(\boldsymbol{r} - \boldsymbol{e}_y d)]/|\boldsymbol{r} - \boldsymbol{e}_y d|. \tag{13}$$

The scattered electric field is approximately of the spatial dependence of that from an image term

$$E_s(\boldsymbol{r}) = \mathrm{s}\exp[i\boldsymbol{k}\cdot(\boldsymbol{r} + \boldsymbol{e}_y d)]/|\boldsymbol{r} + \boldsymbol{e}_y d|, \tag{14}$$

where $\mathrm{s} = \pm 1$, depending on whether one is on the LHS or RHS of the source. For small d, there is an obvious cancellation between these two terms. As d is increased, this cancellation only remain at $y = 0$. But for other values of y, this cancellation becomes too much weaker.

4.2 Frequency dependence of the SAR effect

The MSP resonance occurs at a specified frequency. Accordingly, the SAR effect should be also dependent on the selection of the working frequency. In Fig. 5 (a), we present the photonic

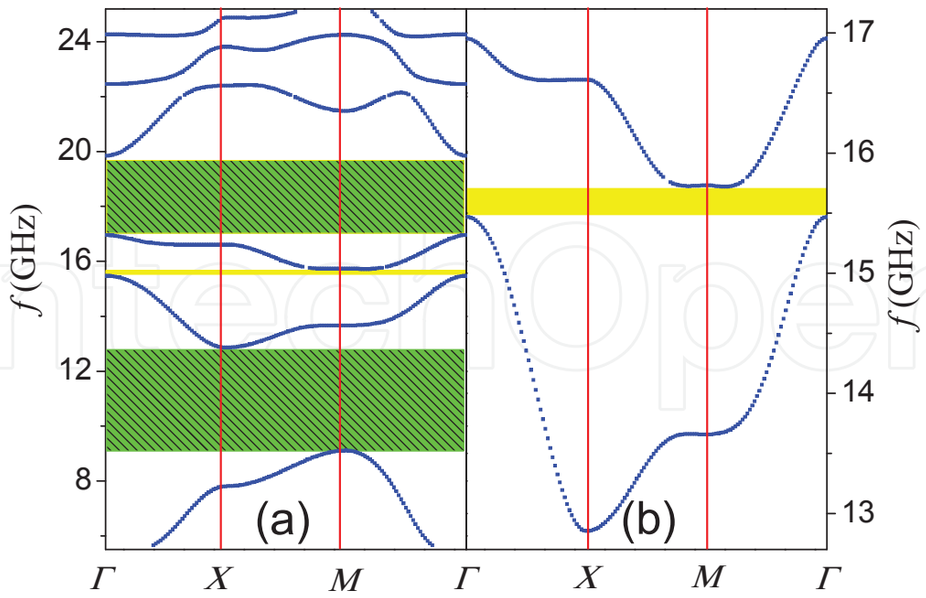

Fig. 5. (a) The photonic band diagram at the higher frequency where three PBGs arising from the bragg scattering can be observed. (b) The amplified view of the photonic band diagram around the second PBG. All the parameters involved are the same as those in Fig. 1.

band diagrams at higher frequencies, where three PBGs are identified. We first examine the reflection behavior at the frequency $f = 9.5$ GHz located at the bottom of the first PBG. The simulation result is shown in Fig. 6 (a), where the field pattern is almost symmetric, no SAR effect can be observed. Presumably, the Chern numbers of the photonic bands nearby are zero, only a tiny circulation of the energy flow occurs so that no significant asymmetry reflection is observed. The result is consistent with that in Wang and coworkers' research where they present the Chern number corresponding to the photonic bands (Wang et al., 2008). Similarly, for the upmost PBG ranging from 17 GHz to 19.5 GHz, the SAR effect can not be observed either due to the same reason. Between these two PBGs, there exist another narrow PBG as denoted by a yellow stripe in Fig. 5 (a). We select a frequency $f = 15.5$ GHz as the working frequency to examine the reflection behavior. For convenience, we have given in Fig. 5 (b) the amplified view of the photonic band diagram around this PBG. The corresponding electric field pattern is shown in Fig. 6 (b) where the electric field on the RHS is nearly vanished near the interface, while on the LHS the electric field can be supported so that the SAR effect comes into appearance. The PBG comes from the degeneracy lift resulting from the gyrotropic anisotropy of the MMs. At this frequency range, the energy circulation can be excited, which we will discuss later on.

For comparison, we have also performed the simulation to examine the reflection behavior of a line source from an MPC slab with the same parameters in Wang and coworkers' research (Wang et al., 2008). Concretely, the lattice constant is $a = 38.7$ mm, the radius of the ferrite rod is $r = 0.11a = 4.3$ mm, the corresponding matrix elements of the magnetic permeability are $\mu = 14$ and $\mu' = -12.4$, the working frequency is $f = 4.28$ GHz, and the line source is located $0.25a$ away from the interface. The electric field pattern is shown in Fig. 6 (c) where the EM wave is reflected somewhat leftwards. A weak asymmetry reflection can be observed. In this case, the Chern numbers of the photonic bands around the PBG are not zero as shown by Wang and coworkers (Wang et al., 2008). However, different from the results shown in Fig.

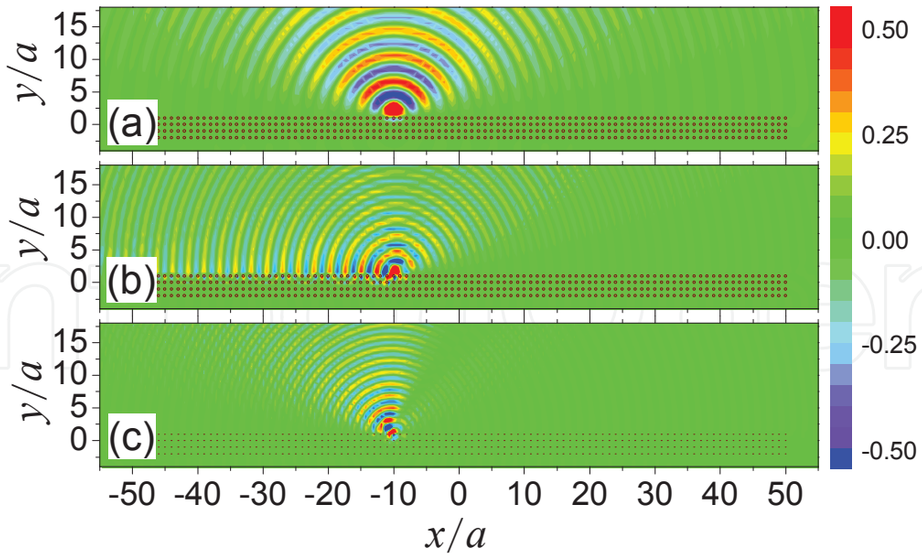

Fig. 6. The reflection behavior for the working frequency located at $f = 9.5$ GHz (a) and $f = 15.5$ GHz (b), corresponding to those in the lower and higher PBGs, respectively, due to the Bragg scattering. The reflection behavior of a line source from an MPC slab with the same parameters in (Wang et al., 2008) is also examined as shown in panel (c).

2, there appears no enhancement of EM field near the interface due to the absence of MSP resonance.

It should be noted that the direction of EM energy circulation does not depend solely on the magnetization, as can be illustrated by comparing Fig. 2 (a) to Fig. 6 (b). To determine the direction of the circulation (clockwise or anticlockwise) we need to calculate the energy circulation around the ferrite rods. For a single rod, it can be evaluated according to

$$\oint \boldsymbol{P} \cdot \mathrm{d}\boldsymbol{l} = A(\omega) \sum_n n \left| \frac{b_n}{q_n} \frac{H_n^{(1)}(x)}{J_n(x)} - 1 \right|^2 |q_n J_n(x)|^2 , \tag{15}$$

where $A(\omega) = \frac{\pi |E_0|^2}{\mu_b \omega}$ is the prefactor with E_0 the amplitude of the incident wave and μ_b the magnetic permeability of the background medium, $x = k_b r_s$ is the size parameter, b_n and q_n are, respectively, the expansion coefficients of the scattered and incident wave corresponding to the angular momentum n, $J_n(x)$ is $n-$th order the Bessel function, and $H_n^{(1)}(x)$ is the $n-$th order Hankel function of the first kind. From Eq. (15), it can be found that the energy circulation depends on the difference of the scattering amplitude for the $|n|$ and the $-|n|$ terms. While the scattering amplitude corresponding to $n = 0$ is not involved. We have calculated the energy circulation around a typical ferrite rod in the first layer of the MM slab. The results show that the circulation is about $-10^{-2} A(\omega)$ for Fig. 2 (a), suggesting a clockwise energy flow, thus explaining the rightwards reflection. For Fig. 6 (a), the energy circulation is nearly zero, corresponding the nearly symmetric reflection. For Fig. 6 (b), the energy circulation is about $10^{-2} A(\omega)$, indicating that an anticlockwise energy flow is formed, explaining the leftwards reflection. While for the case in Fig. 6 (c), the energy circulation is about $10^{-4} A(\omega)$, much weaker than the case in Fig. 2 (a) and Fig. 6 (b). Accordingly, although the leftward reflection occurs, along the interface nearly no EM mode is supported.

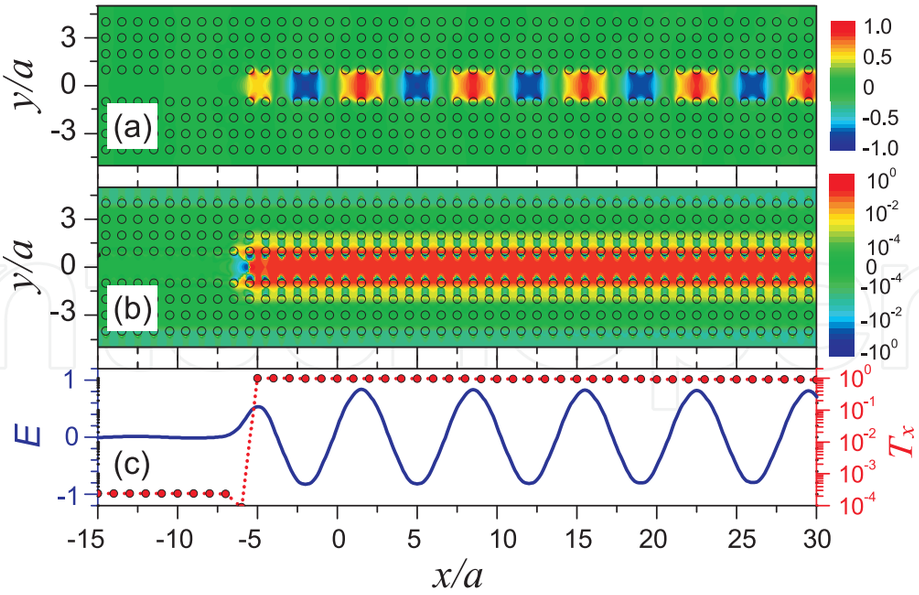

Fig. 7. The profile of the electric field (a) and the x-component of the Poynting vector (b) when a line source of $f = 5$ GHz is located at $(-5.5a, 0)$, between two MM slabs with opposite magnetization and the channel width $D = 2a$. Here $a = 8$ mm is the lattice constant of a square lattice of MM. Panel (c) displays the electric field E at $y = 0$ and the rightward transmitted power T_x versus x as denoted by blue solid line and red dotted line, respectively.

5. Design of an OEMW based on the MSP

Based on the SAR effect we can explore some possible applications. A typical example is due to the remarkable asymmetry of the Poynting vector as shown in Fig. 2 (c). Because of the existence of the PBGs around the MSP resonance, the EM wave can be confined between two MM slabs and transported only in the channel, similar to the conventional photonic crystal waveguide. If two MM slabs have the opposite magnetization, then the EM wave reflected forward from one MM slab will also be reflected forward from the other, leading to the design of an OEMW different from those proposed recently (Fu et al., 2011; 2010; He et al., 2010; Huang & Jiang, 2009; Wang et al., 2008; 2009; Yu et al., 2008; Zhu & Jiang, 2010). The performance of the OEMW is illustrated in Fig. 7 (a) where a line source is placed at $(-5.5a, 0)$, in the middle of two MM slabs with the channel width $D = 2a$. The parameters for the MM slabs and the operating frequency of the line source are the same as in Fig. 2. It can be observed that the EM wave propagates rightward as demonstrated by the x component P_x of the Poynting vector $\boldsymbol{P}$ shown in Fig. 7 (b). To further illustrate the one-way characteristic, we display in Fig. 7 (c) the electric field along $y = 0$ and the rightward transmitted power, $T_x = \int_{-3a}^{3a} P_x \mathrm{d}y$, as the functions of the position x. In addition, the EM energy exhibits an extremely low decay rate that is less than 0.1 dB/λ when taking into account of the realistic material absorption (Pozar, 2004). To search out the physical essence, in the following, we will neglect the damping for simplicity.

5.1 Channel width dependence of the OEMW

As already shown in Fig. 4, the SAR effect is dependent on the source-interface separation and it is only workable when the separation is small. This suggests that the OEMW designed

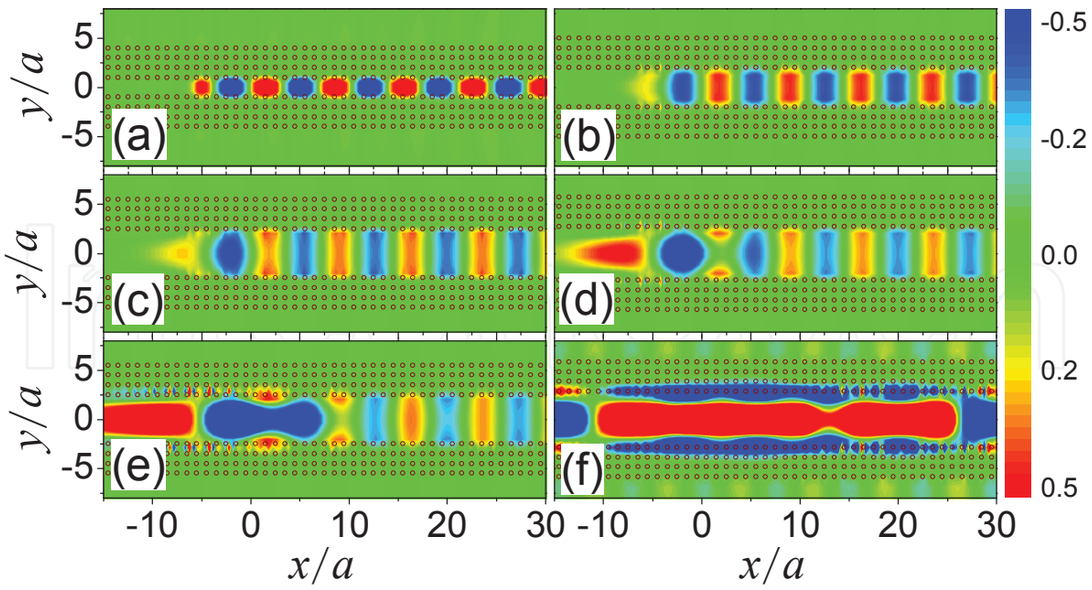

Fig. 8. The electric field patterns for the OEMW operated with different channel widths. Panels (a), (b), (c), (d), (e), and (f) correspond to the cases for the channel widths $D = 2.0a$, $D = 4.0a$, $D = 5.5a$, $D = 5.6a$, $D = 5.7a$, and $D = 6.0a$, respectively.

according to this effect should also depend on the channel width. Physically, as the channel width becomes larger than a wavelength, one part of the EM wave can propagate along the channel without experiencing any of the reflection. Therefore, the unidirectional propagation characteristic shown in Fig. 7 will be diminished. In Fig. 8, we have presented the electric field patterns for the OEMW with different channel widths. Panels (a), (b), (d), (e), and (f) correspond to channel widths $D = 2.0a$, $D = 4.0a$, $D = 5.5a$, $D = 5.6a$, $D = 5.7a$, and $D = 6.0a$, respectively. For OEMW with the channel width $D < 5.5a$, the leftward propagating EM wave is suppressed completely. The OEMW can be considered as a unidirectional device with good performance. However, with the increase of the channel width more and more EM field leaks leftwards as can be observed in Figs. 8 (d)-(f). This result is in good agreement with the result shown in Fig. 4 in that the unidirectionality becomes weaker and weaker with the increase of the source-interface separation. When the channel width is increased to $D = 6.0a$, nearly 0.8λ, no obvious difference can be observed for the leftward and rightward propagating EM waves.

5.2 Robustness against defect, disorder, and inhomogeneity of EMF

A particular important issue of current interest is the robustness of a designed EM devices against defect and disorder. We have performed the simulations to illustrate the issue, which indicates that the one-way waveguiding property based on the SAR effect appears to be immune to defect and disorders, as demonstrated typically in Figs. 9 (b-d). Figure 9 (b) simulates the electric field pattern when a finite linear array of close-packed perfect electrical conductor (PEC) rods is inserted to block the channel. The radius of the PEC rod is $r_p = \frac{1}{2}r_s$. The linear array ranges from $y = -2.5a$ to $y = 2.5a$, forming a drastic defect extending over $\frac{2}{3}\lambda$ in length. The EM wave is seen to circumvent the PEC defect, maintaining a nearly complete power transmission T_x along the channel, as shown in Fig. 9 (j). In Fig. 10, we present a

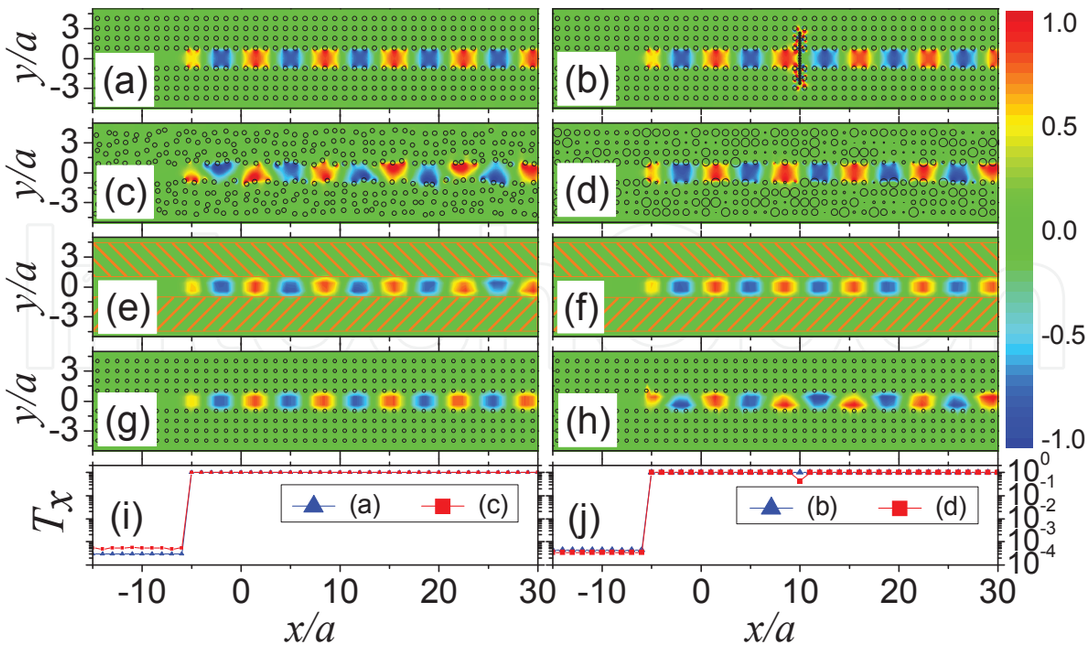

Fig. 9. The electric field patterns for the OEMW operated under the conditions (a) the same as Fig. 7 (a), given here for comparison, (b) with the introduction of a drastic PEC defect to block the channel, (c) with position disorder, and (d) with size fluctuation. The averaged electric field patterns for 20 configurations with position disorder (e) and size fluctuation (f) are also given. The inhomogeneity of the EMF is considered as well for the cases of (g) inhomogeneous and symmetric EMF, and (h) inhomogeneous and asymmetric EMF. In addition, the normalized transmitted power versus x for (a), (c) and (b), (d) are plotted and presented in panels (i) and (j), respectively.

simple schematic diagram to show how the OEMW works and how the EM wave circumvents the PEC defect, which could be helpful for the understanding of mechanism dominating the behavior. For the perfect case without any defect, the MSP resonance can induce the formation of a unidirectional energy circulation so that the channel can only support the energy flow in one direction, the OEMW is thus designed as shown in Fig. 10 (a). When a PEC defect is inserted into the channel, an equivalent waveguiding channel can be created between the PEC defect and the MM as marked by the dashed vertical arrows. Therefore, the EM wave can get around the PEC defect without experiencing any backscattering by propagating along this equivalent channel, resulting in a nearly complete energy transmission. Compared with the defect free waveguide shown in Fig. 9 (a), it can be observed that the defect changes only the phase of the rightward propagating wave, as a result of the delay due to the PEC defect.

The designed OEMW is also robust against the position disorder and the size fluctuation of the ferrite rods as illustrated in Figs. 9 (c) and 9 (d) where we present the corresponding electric field patterns when these two types of perturbations are involved. Position disorder is controlled by a series of random numbers, which introduce a maximal coordinate variation equal to $\frac{1}{4}a$. The size fluctuation of the rod radius is uniform up to 50% of the unperturbed case. It can be observed that the disorder only alters the field patterns, but not the power transmission through the channel as shown in Figs. 9 (i) and (j). Actually, for even stronger perturbation the OEMW still works well provided that the channel is not destroyed. For

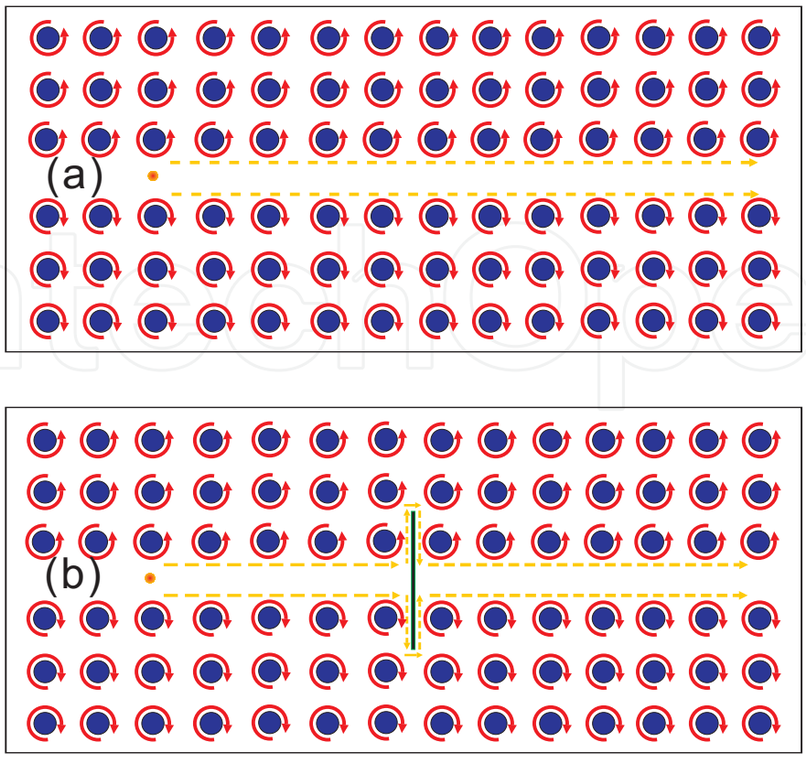

Fig. 10. The simple schematic picture to illustrate how the OEMW works (a), and how the EM wave can get around the defect without any back scattering (b) where the point denote the line source, the circular arrows denote the energy circulation supported by the ferrite rods, and the solid black line denote the PEC defect.

the edge state waveguide, (Wang et al., 2008) the working frequency lies in the Bragg type PBG, so although the system can be immune to the defect, it may suffer from disorder of the building blocks. In Figs. 9 (e) and (f), we also present the averaged electric field patterns over 20 configurations of position and radius disordered systems, respectively. It can be found that the averaged field patterns bear resemblance to that without any perturbation, owing to cancellation of the field at the irregular interface for different configurations. The cases corresponding to different amplitude of perturbation are examined as well, similar behaviors can be observed, indicating the statistical validity of the results.

In realistic situation, the EMF can not be perfectly homogeneous. For this reason, we also present the simulation results for the OEMW operated under an inhomogeneous EMF. Figure 9 (g) corresponds to the case when a symmetric inhomogeneous EMF is exerted. The EMFs at the different layers from inside to outside are, respectively, 890 Oe, 910 Oe, 930 Oe, and 950 Oe, symmetrically for the upper and lower MM slabs. The situation corresponding to the asymmetric inhomogeneous EMF is also considered as shown in Fig. 9 (h) where the EMFs at different layers from inside to outside are 870 Oe, 900 Oe, 910 Oe, 950 Oe for the upper MM slab and 920 Oe, 930 Oe, 940 Oe, 970 Oe for the lower MM slab. It can be observed that the symmetric distribution of the EMF leads to a symmetric electric field pattern and the asymmetric EMF can shape the electric field pattern into an asymmetric one. However, a good performance can still be maintained. This is also a favorable aspect for the design of the EM devices.

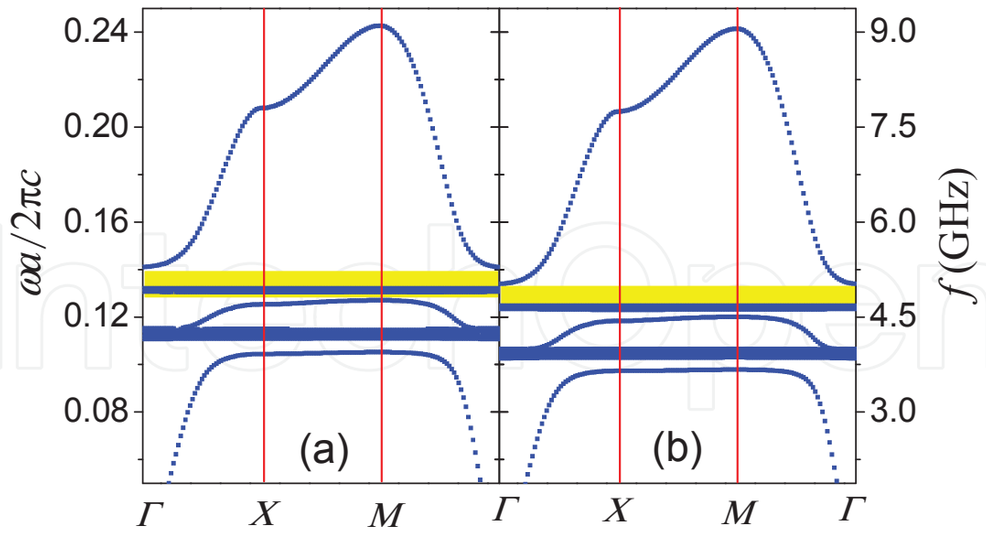

Fig. 11. The photonic band diagrams corresponding to the MM operated under two different EMFs (a) $H_0 = 900$ Oe and (b) $H_0 = 800$ Oe, respectively. The other parameters of the MM are the same as those used in Fig. 1. The working frequency ranges for the OEMW under different EMFs are denoted with the yellow stripes.

5.3 Tunability of the working frequency

A special property of the OEMW designed in our work is the tunability of the working frequency due to the dependence of the MSP resonance on the EMF. This tunability can be clearly seen by examining the photonic band diagrams of the MM under different EMFs as shown in Figs. 11 (a) and (b), corresponding to $H_0 = 900$ Oe and $H_0 = 800$ Oe, respectively. The yellow stripes mark the working frequency range of the OEMW, the flat bands there correspond to the MSP resonance. When the EMF decreases from $H_0 = 900$ Oe to $H_0 = 800$ Oe, the flat bands move downwards, so does the working frequency. In this manner, the working frequency can be controlled by an EMF. Due to the sensitivity of the MSP resonance dependent on the EMF, the working frequency of the OEMW can be manipulated easily.

To give a clear picture how the OEMW works under different EMF, we present in Fig. 12 the electric field patterns of the OEMW under $H_0 = 900$ Oe [(a), (b)] and $H_0 = 800$ Oe [(c), (d)], respectively. The other parameters of the OEMW are the same as those in Fig. 7. In panel (a), the frequency is $f = 5.2$ GHz, lying in the working frequency range. As can be observed, the EM field is confined in the channel and a good one-way propagating behavior is manifested. When the frequency is decreased to $f = 4.7$ GHz under the same EMF, it lies outside the working frequency range, the EM field leaks outside the channel as demonstrated in Fig. 12 (b). Accordingly, the EM field propagating along the channel becomes weaker and weaker so that at this frequency it can not be operated as an OEMW. Nonetheless, by tuning EMF to a lower value $H_0 = 800$ Oe, $f = 4.7$ GHz is located in the new working frequency range as can be confirmed from the photonic band diagram in Fig. 11 (b). The corresponding electric field pattern is shown in Fig. 12 (c) where we can observe that the OEMW works very well. Similar to the case shown in Fig. 12 (b), if the frequency is tuned to $f = 5.2$ GHz, lying outside the working range under $H_0 = 800$ Oe. Then, the device can not be operated as an OEMW by examining the electric field pattern shown in Fig. 12 (d) where we can see that most of the EM field leaks outside the channel. From the above analysis, we can conclude that by tuning the

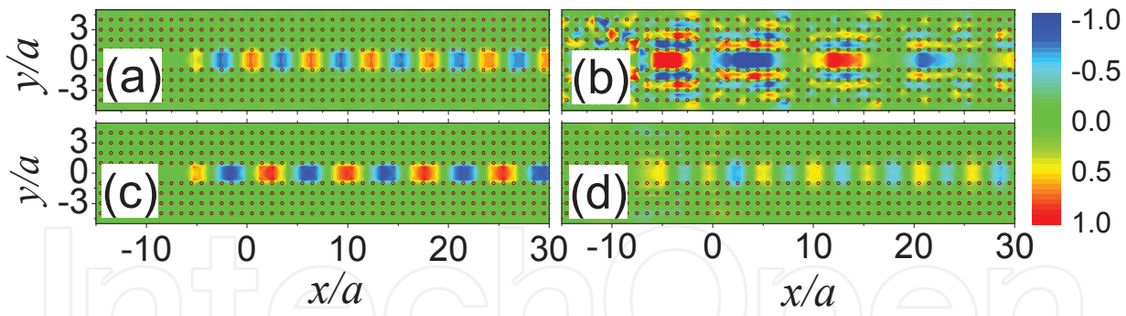

Fig. 12. The electric field patterns showing the OEMW working at frequency $f = 5.2$ GHz (a), (d) and $f = 4.7$ GHz (b), (c). The exerted EMFs are $H_0 = 900$ Oe and $H_0 = 800$ Oe for (a)-(b) and (c)-(d), respectively. All the other parameters are the same as those in Fig. 7.

EMF from $H_0 = 900$ Oe to $H_0 = 800$ Oe, the working frequency can be adjusted from 5.2 GHz to 4.7 GHz. Accordingly, by tuning the EMF we can manipulate the working frequency of the OEMW. However, for the OEMW designed based solely on the TRS breaking, the working frequency is inert to the EMF so that no manipulability can be expected.

6. Design of beam bender and splitter

Based upon the SAR effect, we can also design other EM waveguiding devices by constructing a corner configuration. Typical simulation results of such applications are presented in Fig. 13 where the configuration of the system is similar to that of the OEMW except that a cladding slab is added on top of the system. For a line source located in the vertical channel at $(0, -15a)$, the EM wave is seen to propagate upward first, operated in the same manner as an OEMW. After that, the EM waves make a 90° turn at the corner without any backward scattering so that nearly 100% power transmission is realized for the beam bender, as shown quantitatively in Fig. 13 (e) by the blue solid line. The power transmission rates are defined as T_x/T_y with T_x and T_y the EM energy propagating along the two different parts of the channel in the x (rightward) and the y (upward) directions. They are calculated numerically according to $T_x = \int_{-3a}^{3a} P_x \mathrm{d}y$ and $T_y = \int_{-3a}^{3a} P_y \mathrm{d}x$. By reversing the magnetization of the ferrite rods with the coordinates $x < 0$ in the upper cladding slab, the EM wave can be divided equally into two branches at the bifurcation point $x = 0$ as shown in Fig. 13 (b). In each wing the EM wave is transported with 50% power transmission in some frequency range, as is shown in Fig. 13 (e) by the red dashed line. In the frequency range $f > 5.04$ GHz the power transmission rate for the beam bender decreases obviously as can be observed in Fig. 13 (e). To explain this, we have presented the electric field patterns for the beam bender and splitter operated at the frequency $f = 5.1$ GHz. The results are shown in Figs. 13 (c) and (d), respectively. For the beam bender, due to the difference of the light path at the upper and lower interfaces the wave front is severely distorted. In addition, as the frequency deviates from the MSP resonance, the energy circulation around the ferrite rods becomes weaker. Therefore, some part of the EM wave leaks leftwards as shown in Fig. 13 (c), resulting in the drop of the transmission rate. Since the orientation of the magnetization can be controlled by an EMF, the function of the system can be switched between bender and splitter. This makes the device more flexible and favorable in practical applications.

The unidirectional waveguiding device designed in our work can still be operable with a good performance in a deep subwavelength scale. In Fig. 14, we present the simulation results. The

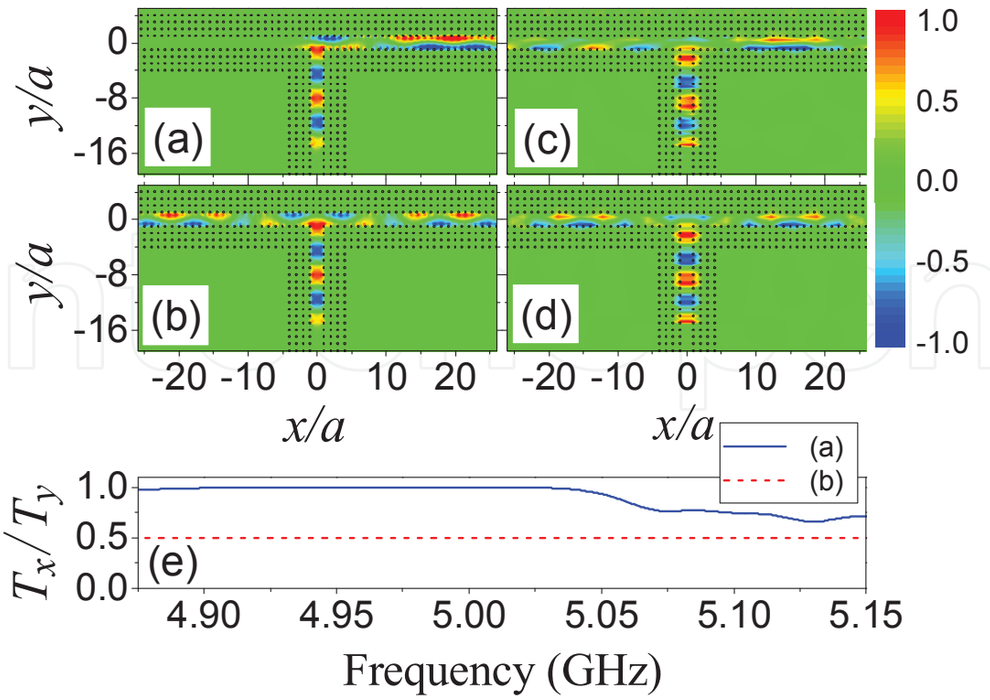

Fig. 13. The simulated electric field patterns corresponding to a 90° shaper beam bender (a) and a beam splitter (b) operating at $f = 5$ GHz under the EMF $H_0 = 900$ Oe. The electric field patterns for the beam bender and splitter working at $f = 5.1$ GHz are also presented in panels (c) and (d), respectively. The lattice constant is $a = 8$ mm, kept unchanged and the line source is located at $(0, -15a)$. The curves in (e) give the transmissivity T_x/T_y plotted as the functions of frequency.

waveguiding device considered in panels (a), (b), and (c) are designed in the same manner as those in Figs. 7 (a), 13 (a), and 13 (b), respectively, except that the MM is scaled down in size, with $a = 2$ mm and $r = \frac{1}{4}a$, while keeping the working frequency $f = 5$ GHz unchanged. In such situation, the working wavelength $\lambda = 60$ mm is nearly 30 times the lattice constant a. It can be observed from the field patterns that a superior subwavelength confining and steering is realized in a straight OEMW, a sharp beam bender, and a beam splitter. The numerical calculations indicate that the full lateral width at half maximum field intensity $w_h < 0.1\lambda$. The power transmissivity is also simulated for the beam bender and splitter as shown in Fig. 14 (d) where the red dashed line and the blue solid line correspond to panels (b) and (c), respectively. It can be seen that the waveguiding devices still exhibit a high transmission efficiency as well as a finite band width. In addition, compared with the results shown in Fig. 13 (e), it can be seen that a shift of the working frequency is demonstrated, which originates from the enhancement of the coupling strength due to the decrease of the lattice separation. Comparing with the results shown in Fig. 13, we can also find that the transmission efficiency for the beam bender is much improved. The reason lies in that the decrease of the channel width will ease up the distortion of the EM field, which is clearly demonstrated in Fig. 14 (b). Accordingly, the power leakage of the EM wave to the left wing of the horizonal channel can be decreased. Besides, just like the case shown in Fig. 13 the function of the system is still magnetically switchable between beam bender and splitter.

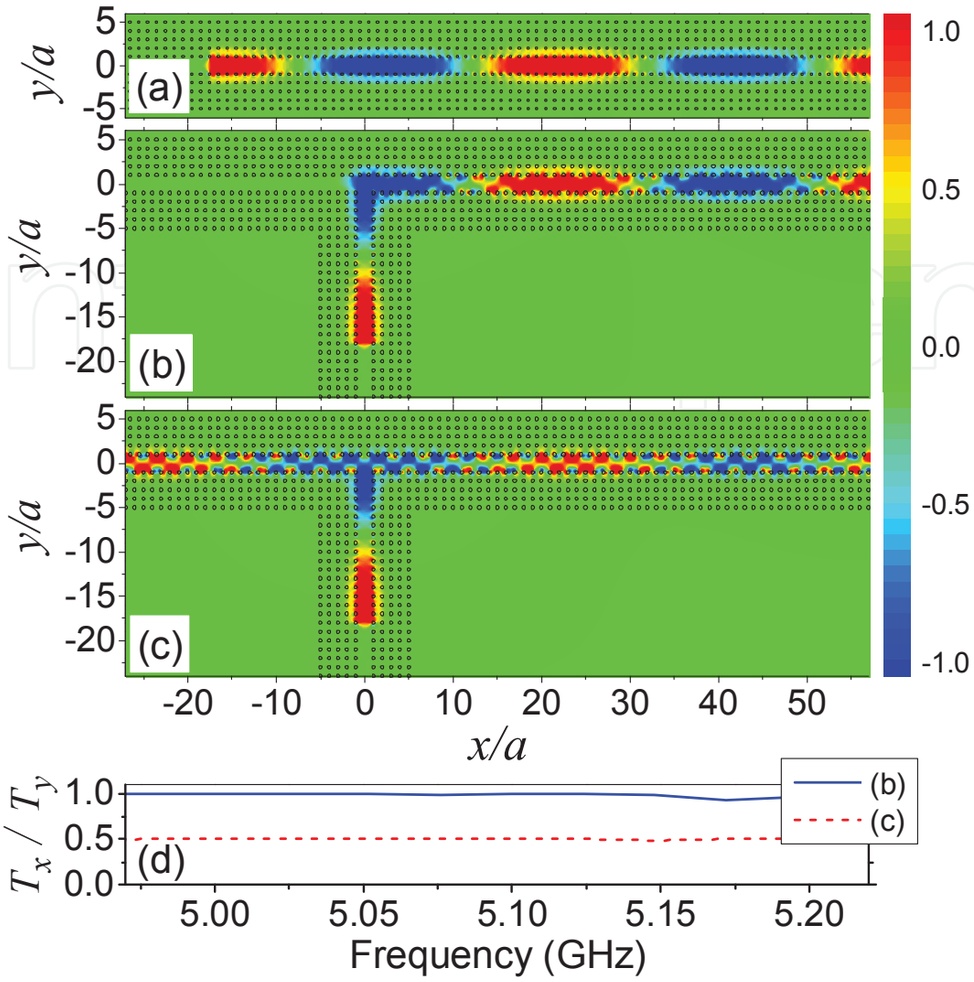

Fig. 14. The electric field patterns showing the device operable at the deep subwavelength scale. Panels (a), (b), and (c) are the same as Fig. 7(a), Fig. 13(a), and Fig. 13(b), respectively, except that the lattice constant of the MM is $a = 2$ mm and rod radius $r = \frac{1}{4}a$. The curves in (d) gives the rightward transmissivity for the beam bender and beam splitter.

7. Conclusion

In summary, we have demonstrated a very interesting SAR effect occurring at the interface of an MM slab. The Mie theory and the multiple scattering theory used in our simulation have also been introduced. Our results suggest that the SAR effect originates from combined action of MSP resonance and TRS breaking nature of MM under an EMF. We also examine the dependence of SAR effect on the frequency and the source-interface separation. Possible applications have been demonstrated by designing a straight OEMW, a sharp beam bender, and a beam splitter. An excellent performance of the device can be achieved. In particular, our design can even be operable in the deep subwavelength scale. Actually, a lot more issues can be expected with appropriate design of the MM such as the muti-channel unidirectional filter, cloaking, and also the zero index materials.

8. Acknowledgements

This work is supported by the China 973 program, NNSFC (10774028, 10904020), MOE of China (B06011), SSTC (08dj1400302), China postdoctoral science foundation (200902211), the open project of SKLSP in Fudan Univeristy (KL2011_8), Zhejiang Provincial Natural Science Foundation of China (Y12A040009) and Zhejing Normal University initiative foundation. STC is partly supported by the DOE.

9. References

Ao, X. Y.; Lin, Z. F. & Chan, C. T. (2009). One-way edge mode in a magneto-optical honeycomb photonic crystal. *Phys. Rev. B*, Vol. 80, No. 3, 033105

Barnes, W. L.; Dereux, A.; Ebbesen, T. W. (2003). Surface plasmon subwavelength optics. *Nature*, Vol. 424, No. 6950, 824-830

Bohren, C. F. & Huffman, D. R. (1983). *Absorption and Scattering of Light by Small Particles*, Wiley, New York.

Burgos, S. P.; Waele, R. de; Polman, A. & Atwater, H. A. (2010). A single-layer wide-angle negative-index metamaterial at visible frequencies. *Nat. Mater.* Vol. 9, No. 5, 407-412

Chen, P.; Wu, R. X.; Xu J.; Jiang, A. M. & Ji, X. Y. (2007). Effect of magnetic anisotropy on the stop band of ferromagnetic band gap materials. *J. Phys.: Condens. Matter*, Vol. 19, No. 10, 106205

Chew, W. C. (1995). *Waves and Fields in Inhomogenous Media*, IEEE Press, New York.

Chui, S. T. & Lin, Z. F. (2007). Probing states with macroscopic circulations in magnetic photonic crystals. *J. Phys.: Condens. Matter*, Vol. 19, No. 40, 406233

Chui, S. T.; Liu, S. Y. & Lin Z. F. (2010). Reflected wave of finite circulation from magnetic photonic crystals. *J. Phys.: Condens. Matter*, Vol. 22, No. 18, 182201

Dolling, G.; Enkrich, C.; Wegener, M.; Soukoulis, C. M. & Linden, S. (2006). Simultaneous negative phase and group velocity of light in a metamaterial. *Science*, Vol. 312, No. 5775, 892-894

Eggimann, W. H. (1960). Scattering of a plane wave on a ferrite cylinder at normal incidence. *IRE Trans. Microwave Theory and Tech.*, Vol. 8, No. 4, 440-445

Engheta, N. (2007). Circuits with light at nanoscales: Optical nanocircuits inspired by metamaterials. *Science*, Vol. 317, No. 5845, 1698-1702

Ergin, T.; Stenger, N.; Brenner, P.; Pendry, J. B. & Wegener, M. (2010). Three-dimensional invisibility cloak at optical wavelengths. *Science*, Vol. 328, No. 5976, 337-339

Fang, N.; Lee, H.; Sun, C. & Zhang, X. (2005). Sub-diffraction-limited optical imaging with a silver superlens. *Science*, Vol. 308, No. 5721, 534-537

Felbacq, D.; Tayeb, G. & Maystre, D. (1994). Scattering by a random set of parallel cylinders. *J. Opt. Soc. Am. A*, Vol. 11, No. 9, 2526-2538

Fu, J. X.; Lian, J.; Liu, R. J.; Guan, L. & Li, Z. Y. (2011). Unidirectional channel-drop filter by one-way gyromagnetic phtonic crystal waveguides. *Appl. Phys. Lett.*, Vol. 98, No. 21, 211104

Fu, J. X.; Liu, R. J.; & Li, Z. Y. (2011). Robust one-way modes in gyromagnetic photonic crystal waveguides with different interfaces. *Appl. Phys. Lett.*, Vol. 97, No. 4, 041112

Giannini,V.; Vecchi, G. & Rivas, J. G. (2010). Lighting up multipolar surface plasmon polaritons by collective resonances in arrays of nanoantennas. *Phys. Rev. Lett.*, Vol. 105, No.26, 266801

Gollub, J. R.; Smith, D. R.; Vier, D. C.; Perram, T.; Mock, J. J. (2005). Experimental characterization of magnetic surface plasmons on metamaterials with negative permeability. *Phys. Rev. B*, Vol. 71, No. 19, 195402

Haldane, F. D. M. & Raghu, S. (2008). Possible realization of directional optical waveguides in photonic crystals with broken time-reversal symmetry. *Phys. Rev. Lett.*, Vol. 100, No. 1, 013904

He, C.; Chen, X. L.; Lu, M. H.; Li, X. F.; Wan, W. W.; Qian, X. S.; Yin, R. C. & Chen, Y. F. (2010). Tunable one-way cross-waveguide splitter based on gyromagnetic phtonic crystal. *Appl. Phys. Lett.*, Vol. 96, No. 11, 111111

Huang, C. & Jiang, C. (2009). Nonreciprocal photonic crystal delay waveguide. *J. Opt. Soc. Am. B*, Vol. 26, No. 10, 1954-1958

Jin, J. J.; Liu, S. Y.; Lin, Z. F. & Chui, S. T. (2009). Effective-medium theory for anisotropic magnetic metamaterials. *Phys. Rev. B*, Vol. 80, No. 11, 115101

Leonhardt, U. (2006). Optical conformal mapping. *Science*, Vol. 312, No. 5781, 1777-1780

Lezec, H. J.; Dionne, J. A. & Atwater, H. A. (2007). Negative refraction at visible frequencies. *Science*, Vol. 316, No. 5823, 430-432

Lai, Y.; Chen, H. Y.; Zhang, Z. Q. & Chan, C. T. (2009). Complementary media invisibility cloak that cloaks objects at a distance outside the cloaking shell. *Phys. Rev. Lett.*, Vol. 102, No. 9, 093901

Leung, K. M. & Qiu, Y (1993). Multiple-scattering calculation of the two-dimensional phtonic band structure. *Phys. Rev. B*, Vol. 48, No. 11, 7767-7771

Li, J. & Pendry, J. B. (2008). Hiding under the carpet: A new strategy for cloaking. *Phys, Rev. Lett.*, Vol. 101, No. 20, 203901

Liu S. Y. & Lin, Z. F. (2006). Opening up complete photonic bandgaps in three-dimensional photonic crystals consisting of biaxial dielectric spheres. *Phys. Rev. E*, Vol. 73, No. 6, 066609

Liu, Z. W.; Lee, H.; Xiong, Y.; Sun, C. & Zhang, X. (2007). Far-field optical hyperlens magnifying sub-diffraction-limited objects. *Science*, Vol. 315, No. 5819, 1686

Liu, S. Y.; Chen, W. K.; Du, J. J.; Lin, Z. F.; Chui, S. T. & Chan, C. T. (2008). Manipulating negative-refractive behavior with a magnetic field. *Phys. Rev. Lett.*, Vol. 101, No. 15, 157407

Liu, S. Y.; Du, J. J.; Lin, Z. F.; Wu, R. X. & Chui S. T. (2008). Formation of robust and completely tunable resonant photonic band gaps. *Phys. Rev. B*, Vol. 78, No. 15, 155101

Liu, R.; Ji, P. C.; Mock, J.; Chin, J. J. Y.; Cui, T. J. & Smith, D. R. (2009). Broadband ground-plane cloak. *Science*, Vol. 323, No. 5912, 366-369

Liu, S. Y.; Lu, W. L.; Lin, Z. F. & Chui, S. T. (2010). Magnetically controllable unidirectional electromagnetic waveguiding devices designed with metamaterials. *Appl. Phys. Lett.*, Vol. 97, No. 20, 201113

Liu, S.Y.; Lu, W. L.; Lin, Z. F. & Chui, S. T. (2011). Molding reflection from metamaterials based on magnetic surface plasmons. *Phys. Rev. B*, Vol. 84, No.4, 045425

Noginov, M. A.; Zhu, G.; Mayy, M.; Ritzo, B. A.; Noginova, N. & Podolskiy, V. A. (2008). Stimulated emission of surface plasmon polaritons. *Phys. Rev. Lett.*, Vol. 101, No. 22, 226806

Ozbay, E.(2006). Plasmonics: Merging photonics and electronics at nanoscale dimensions. *Science*, Vol. 311, No. 5758, 189-193

Pendry, J. B. (2000). Negative refraction makes a perfect lens. *Phys. Rev. Lett.*, Vol. 85, No. 18, 3966-3969

Pendry, J. B.; Holden, A. J.; Stewart, W. J. & Youngs, I. (1996). Extremely low frequency plasmons in metallic mesostructures. *Phys. Rev. Lett.*, Vol. 76, No. 25, 4773-4776

Pendry, J. B.; Holden, A. J.; Holden, D. J. & Stewart, W. J. (1999). Magnetism from conductors and enhanced nonlinear phenomena. *IEEE Tran. Microwave Theory Tech.*, Vol. 47, No. 11, 2075-2084

Pendry, J. B.; Schurig, D. & Smith, D. R. (2006). Controlling electromagnetic fields. *Science*, Vol. 312, No. 5781, 1780-1782

Pozar, D. M. (2004). *Microwave Engineering*, Wiley, New York.

Poo, Y.; Wu, R. X.; Lin, Z. F.; Yang, Y. & Chan, C. T. (2011). Experimental realization of self-guiding unidirectional electromagnetic edge states. *Phys. Rev. Lett.*, Vol. 106, No. 9, 093903

Schurig, D.; Mock, J. J.; Justice, B. J.; Cummer, S. A.; Pendry, J. B.; Starr, A. F. & Smith, D. R. (2006). Metamaterial electromagnetic cloak at microwave frequencies. *Science*, Vol. 314, No. 5801, 977-980

Shalaev, V. M. (2007). Optical negative-index metamaterials. *Nature Photon.*, Vol. 1, No. 1, 41-48

Shelby, R. A.; Smith, D. R. & Schultz S. (2001). Experimental verification of a negative index of reflection. *Science*, Vol. 292, No. 5514, 77-79

Slichter, C. P. (1978) *Principle of Magnetic Resonance*, Springer, Berlin.

Smith, D. R.; Padilla, W. J.; Vier, D. C.; Nemat-Nasser, S. C. & Schultz, S. (2000). Composite medium with simultaneously negative permeability and permittivity. *Phys. Rev. Lett.*, Vol. 84, No. 18, 4184-4187

Taubner, T.; Korobkin, D.; Urzhumov, Y.; Shvets, G. & Hillenbrand, R. (2006). Near-field microscopy through a SiC superlens. *Science*, Vol. 313, No. 5793, 1595

Valentine, J.; Zhang, S.; Zentgraf, T.; Ulin-Avila, E.; Genov, D. A.; Bartal, G. & Zhang, X. (2008). Three-dimensional optical metamaterial with a negative refractive index. *Nature*, Vol. 455, No. 7211, 376-379

Veselago, V. G. (1968). The electrodynamics of substrates whith simultaneously negative values of ε and μ. *Sov. Phys. Usp.*, Vol. 10, No. 4, 509-514

Wang, X. D.; Zhang, X. G.; Yu, Q. L. & Harmon, B. N. (1993). Multiple-scattering theory for electromagnetic waves. *Phys. Rev. B*, Vol. 47, No. 8, 4161-4167

Wang, Z.; Chong, Y. D.; Joannopoulos, J. D. & Soljačić, M. (2008). Reflection-free one-way edge modes in a gyromagnetic photonic crystal. *Phys. Rev. Lett.*, Vol. 100, No. 1, 013905

Wang, Z.; Chong, Y. D.; Joannopoulos, J. D. & Soljačić, M. (2009). Observation of unidirectional backscattering-immune topological electromagnetic states. *Nature*, Vol. 461, No. 7265, 772-775

Yu, Z. F.; Veronis, G.; Wang, Z. & Fan, S. H. (2008). One-Way electromagnetic waveguide formed at the interface between a plasmonic metal under a static magnetic field and a photonic crystal. *Phys. Rev. Lett.*, Vol. 100, No. 2, 023902

Zayats, A. V.; Smolyaninov, I. I. & Maradudin, A. A. (2005). Nano-optics of surface plasmon polaritons. *Phys. Rep.*, Vol. 408, No. 3-4, 131-314

Zentgraf, T.; Liu, Y. M.; Mikkelsen, M. H.; Valentine, J. & Zhang, X. (2011). Plasmonic Luneburg and Eaton lenses. *Nat. Nanotechnology*, Vol. 6, No. 3, 151-155

Zhang, S.; Fan, W.; Panoiu, N. C.; Malloy, K. J.; Osgood, R. M. & Brueck, S. R. J. (2005). Experimental demonstration of near-infrared negative-index metamaterials. *Phys. Rev. Lett.*, Vol. 95, No. 13, 137404

Zhu, H. B. & Jiang, C. (2010). Broadband unidirectional electromagnetic mode at interface of anti-parallel magnetized media. *Opt. Express*, Vol. 18, No. 7, 6914-6921

Zia, R.; Schuller, J. A.; Chandran, A. & Brongersma, M. L. (2006). Plasmonics: the next chip-scale technology. *Materials today*, Vol. 9, No. 7-8, 20-27

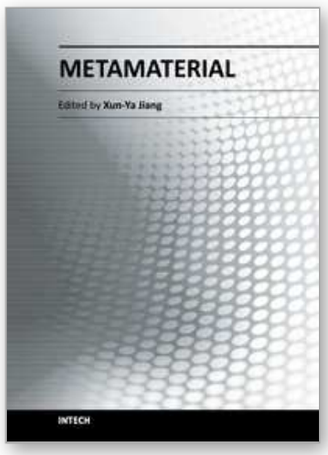

Metamaterial

Edited by Dr. Xun-Ya Jiang

ISBN 978-953-51-0591-6
Hard cover, 620 pages
Publisher InTech
Published online 16, May, 2012
Published in print edition May, 2012

In-depth analysis of the theory, properties and description of the most potential technological applications of metamaterials for the realization of novel devices such as subwavelength lenses, invisibility cloaks, dipole and reflector antennas, high frequency telecommunications, new designs of bandpass filters, absorbers and concentrators of EM waves etc. In order to create a new devices it is necessary to know the main electrodynamical characteristics of metamaterial structures on the basis of which the device is supposed to be created. The electromagnetic wave scattering surfaces built with metamaterials are primarily based on the ability of metamaterials to control the surrounded electromagnetic fields by varying their permeability and permittivity characteristics. The book covers some solutions for microwave wavelength scales as well as exploitation of nanoscale EM wavelength such as visible specter using recent advances of nanotechnology, for instance in the field of nanowires, nanopolymers, carbon nanotubes and graphene. Metamaterial is suitable for scholars from extremely large scientific domain and therefore given to engineers, scientists, graduates and other interested professionals from photonics to nanoscience and from material science to antenna engineering as a comprehensive reference on this artificial materials of tomorrow.

How to reference

In order to correctly reference this scholarly work, feel free to copy and paste the following:

Shiyang Liu, Huajin Chen, Zhifang Lin and S. T. Chui (2012). Magnetically Tunable Unidirectional Electromagnetic Devices Based on Magnetic Surface Plasmon, Metamaterial, Dr. Xun-Ya Jiang (Ed.), ISBN: 978-953-51-0591-6, InTech, Available from: http://www.intechopen.com/books/metamaterial/magnetically-tunable-unidirectional-electromagnetic-devices-based-on-magnetic-surface-plasmon

INTECH
open science | open minds

InTech Europe
University Campus STeP Ri
Slavka Krautzeka 83/A
51000 Rijeka, Croatia
Phone: +385 (51) 770 447
Fax: +385 (51) 686 166
www.intechopen.com

InTech China
Unit 405, Office Block, Hotel Equatorial Shanghai
No.65, Yan An Road (West), Shanghai, 200040, China
中国上海市延安西路65号上海国际贵都大饭店办公楼405单元
Phone: +86-21-62489820
Fax: +86-21-62489821

IntechOpen